PHYSICAL REVIEW E **86**, 046703 (2012)

Numerical simulations of Hall-effect plasma accelerators on a magnetic-field-aligned mesh

Ioannis G. Mikellides[*] and Ira Katz

Jet Propulsion Laboratory, California Institute of Technology, Pasadena, California 91109, USA

(Received 7 June 2012; published 17 October 2012; publisher error corrected 24 October 2012)

The ionized gas in Hall-effect plasma accelerators spans a wide range of spatial and temporal scales, and exhibits diverse physics some of which remain elusive even after decades of research. Inside the acceleration channel a quasiradial applied magnetic field impedes the current of electrons perpendicular to it in favor of a significant component in the $\mathbf{E} \times \mathbf{B}$ direction. Ions are unmagnetized and, arguably, of wide collisional mean free paths. Collisions between the atomic species are rare. This paper reports on a computational approach that solves numerically the 2D axisymmetric vector form of Ohm's law with no assumptions regarding the resistance to classical electron transport in the parallel relative to the perpendicular direction. The numerical challenges related to the large disparity of the transport coefficients in the two directions are met by solving the equations on a computational mesh that is aligned with the applied magnetic field. This approach allows for a large physical domain that extends more than five times the thruster channel length in the axial direction and encompasses the cathode boundary where the lines of force can become nonisothermal. It also allows for the self-consistent solution of the plasma conservation laws near the anode boundary, and for simulations in accelerators with complex magnetic field topologies. Ions are treated as an isothermal, cold (relative to the electrons) fluid, accounting for the ion drag in the momentum equation due to ion-neutral (charge-exchange) and ion-ion collisions. The density of the atomic species is determined using an algorithm that eliminates the statistical noise associated with discrete-particle methods. Numerical simulations are presented that illustrate the impact of the above-mentioned features on our understanding of the plasma in these accelerators.

DOI: 10.1103/PhysRevE.86.046703 PACS number(s): 02.70.−c, 52.65.−y, 52.75.−d, 52.80.−s

I. INTRODUCTION

The numerical simulation of Hall-effect plasma accelerators, commonly also referred to as Hall thrusters, spans more than two decades. The first theoretical models of the partially ionized gas in the stationary plasma thruster (SPT) were reported in the 1970s by Morozov and colleagues [1–3]. Hirakawa and Arakawa [4] developed one of the first numerical models of a SPT in three dimensions. Electrons and singly charged ions were simulated using a particle-in-cell (PIC) scheme that was combined with a Monte Carlo collision model. The electric field was determined by solving Poisson's equation. A computational approach that has been used extensively in the last two decades is to solve the fluid (inertialess) momentum and energy conservation laws for the electrons but use discrete-particle methods to track the evolution of the heavy species. This "hybrid" approach allowed for the capture of bulk plasma phenomena and ion kinetics in the thruster within reasonable computational times and, as a result, it gained considerable popularity. One of the first models to follow this approach was developed by Fife [5]. The model, dubbed "HPHall" (hybrid-PIC Hall), uses a PIC-direct simulation Monte Carlo (DSMC) method for ions in two-dimensional (2D) axisymmetric geometry and it appears that it was the first to reproduce the so-called breathing mode oscillations in Hall thrusters, in two dimensions. Interpretations of these oscillations were provided around the same time by Fife *et al.* using an idealized zero-dimensional (0D) model [6], and by Boeuf and Garrigues [7] using a one-dimensional (1D) time-dependent model with a hybrid treatment of electrons and ions. A 1D generalization of Fife's 0D solution was also derived later by Barral and Ahedo [8]. In Fife's work a model for anomalous electron mobility was employed in the original SPT simulations that was based on Bohm's scaling [9] for the anomalous collision frequency, $\nu_B \sim B/16$. The precise numerical value used in the simulations was guided by experiments. Since the late 1990s HPHall has been used to simulate several other thrusters and, naturally, its numerical and physical models have undergone several improvements and extensions. Recently the model was upgraded to HPHall(2) by Parra and Ahedo [10]. A hybrid approach has been followed also by Sommier *et al.* [11] and by Hagelaar *et al.* [12]. Instead of Bohm diffusion Hagelaar used empirical parameters to account for additional anomalous electron transport and energy loss phenomena [13]. It is interesting to note that despite the apparent popularity of the hybrid approach in recent years, the earliest attempts to model the heavy species followed purely hydrodynamic formalisms [14] (and references therein). A hydrodynamic approach for the heavy species in the thruster was also applied later by Keidar *et al.* [15], but only the ions were solved for in two dimensions.

Because the fundamental principle behind the acceleration of ions in the Hall thruster chamber is based on operation at high electron Hall parameter ($\Omega_e > 100$), the resistance to the transport of mass and heat in the electron flow in the direction perpendicular to the magnetic field is much greater (by $\sim \Omega_e^2$) than that in the parallel direction for most of the channel region. This allows one to solve the full partial differential transport equations only in a direction that is perpendicular to the magnetic field; in the parallel direction the electron equations are simplified by assuming constant temperature and an algebraic equation for the plasma potential. Hereinafter we shall call this simplification the "quasi-1D assumption." Numerically, the assumption allows for the discretization of the electron equations in a quadrilateral computational cell that

---

[*] Corresponding author: ioannis.g.mikellides@jpl.nasa.gov

is bounded by two adjacent lines of force rather than one with arbitrary dimensions. This is the approach followed in HPHall.

Modeling regions of the thruster with complex magnetic field arrangements (such as those near eroded walls and magnets) and/or reduced Hall parameter (such as those near the anode and the cathode plume) challenge the applicability of the quasi-1D assumption. In this article we present a 2D computational model of the partially ionized gas in a Hall thruster that employs the full vector form of Ohm's law. No assumptions are made regarding the rate of electron transport in the parallel and perpendicular directions of the magnetic field. Excessive numerical diffusion due to the large disparity of the transport coefficients in the two directions is avoided by solving the equations on a computational mesh that is aligned with the applied magnetic field. Employment of magnetic field-aligned meshes (MFAM) is a long-standing computational approach for simulating highly anisotropic plasmas, and is widely used nowadays especially by the sustained fusion energy community [16–19]. Field-aligned meshing was also attempted in early versions of a 2D model of the discharge chamber in an ion engine. It was found that the complexity of the magnetic field near the ring cusps made the mesh generation prohibitively sensitive to small changes in the magnetic field strength or geometry. This made the application of the model to realistic thruster arrangements cumbersome, so the MFAM was eventually replaced with a simpler orthogonal mesh [20]. Other non-MFAM approaches to overcome the numerical errors associated with the extreme anisotropy of the electron transport have also been reported. For example, Hagelaar [21] developed the *transverse-flux method*, in which the electron-flux components of the anisotropic drift-diffusion equation are calculated in an iterative manner from the longitudinal gradients and the transverse-flux component (rather than from the longitudinal and transverse gradients) on a mesh that is not aligned with the magnetic field. The method yielded accurate electron fluxes and correct potential profiles in a wide range of numerical experiments.

The computation model presented here also incorporates an algorithm that solves for the density of the collisionless gas. The algorithm is based on line-of-site formulations thereby eliminating the inherent statistical fluctuations of conventional particle methods [22]. Ions are modeled using a fully hydrodynamic approach that, in addition to the inelastic collision terms associated with the ionization, retains in the momentum equation the ion pressure and the ion drag force associated with ion-neutral charge-exchange and ion-ion Coulomb collisions. Hereinafter we shall call the newly developed model Hall2De (with "2De" referring to electron flow in two dimensions, parallel and perpendicular to the magnetic field).

The article is organized as follows. Section II provides a brief description of the thruster's operational principle (Sec. II A), some relevant background regarding the computational approach (Sec. II B), and a description of the governing physics laws and numerical methodologies for the ions (Sec. II C), electrons (Sec. II D), and atomic species (Sec. II E). Section III provides results from benchmark numerical simulations of a commercial Hall thruster [23]. The results are compared with those from HPHall simulations [24] of the same thruster.

II. GOVERNING PHYSICS LAWS AND NUMERICAL METHODOLOGIES

A. Operational principle of the accelerator

Since its inception, detailed theoretical investigations by Morozov between 1963 and 1969 and subsequent experimental studies in the 1970s (see [1] and references therein), the fundamental principle of operation of the Hall thruster, also known as the "closed-drift accelerator," remains unchanged today. A schematic illustrating some of the basic components and features in a SPT-type thruster is shown in Fig. 1. The distinctive principle of operation in these accelerators lies in the applied magnetic field strength and low density of electrons in the annulus which is typically called the acceleration channel. A magnetic system, usually consisting of coils and magnetic poles, produces a quasiradial magnetic field with such strength that the radius of gyration, $r_g = m|\mathbf{u} \times \mathbf{B}|/qB^2$, for electrons is much smaller than the channel length L whereas the gyration radius for ions is much larger than L, that is,

$$\bar{r}_e \ll 1 \ll \bar{r}_i, \tag{1}$$

where $\bar{r} \equiv r_g/L$ and m, q, and $\mathbf{u}$ are the mass, charge, and drift velocity of the particle respectively. $\mathbf{B}$ is the magnetic induction vector field. Unless otherwise noted, throughout this article subscripts e, i, and n will denote electrons, ions, and neutrals, respectively. Electrons are supplied to the acceleration channel by an electron source (usually a thermionic hollow cathode) that is located at the side or at the center of the thruster. If the density of electrons is low, collisions in the azimuthal direction seldom impede their $\mathbf{E} \times \mathbf{B}$ drift resulting in a significant flow of current—the Hall current—in this direction. Operation under these conditions implies a high value of the Hall parameter $\Omega_e \equiv \omega_{ce}/\nu_e$ for the electrons:

$$\Omega_e \gg 1, \tag{2}$$

where ω_{ce} and ν_e are the electron cyclotron and total collision frequencies, respectively. As the Hall current crosses $\mathbf{B}$ the induced electric field $\mathbf{E}$ is in a direction perpendicular to it. According to Ohm's law it is proportional to

$$\mathbf{E}_\perp = \hat{\boldsymbol{\beta}} \times (\mathbf{E} \times \hat{\boldsymbol{\beta}}) \sim \hat{\boldsymbol{\beta}} \times \left(\frac{\mathbf{j}_{e\wedge} \times \mathbf{B}}{q_e n_e} \right) \sim \eta \Omega_e^2 \mathbf{j}_{e\perp}. \tag{3}$$

This electric field serves as the main accelerating force on the ions. In Eq. (3) subscript $\perp$ denotes direction perpendicular to $\mathbf{B}$ and $\wedge$ is in the cross-field direction, where $\hat{\boldsymbol{\beta}} \equiv \mathbf{B}/|\mathbf{B}|$. The electron current density, number density, and resistivity are denoted by $\mathbf{j}_e$, n_e, and η, respectively. Implied in Eq. (3) is that $\mathbf{E}_\wedge = 0$.

Ions are generated largely by electron-impact ionization of the propellant atoms. The propellant, usually xenon, is supplied into the acceleration channel and to the cathode through gas feeds as shown in Fig. 1. The electrons from the cathode as well as those produced by ionization are transported to the anode by a variety of classical and (arguably) nonclassical mechanisms some of which continue to be the subject of extensive research today. Hereafter, by "classical" we shall refer to binary elastic and inelastic collisions between particles whereas all other processes that may contribute to the diffusion of electrons, including scattering by waves and collisions with walls, shall be termed "nonclassical" or "anomalous."

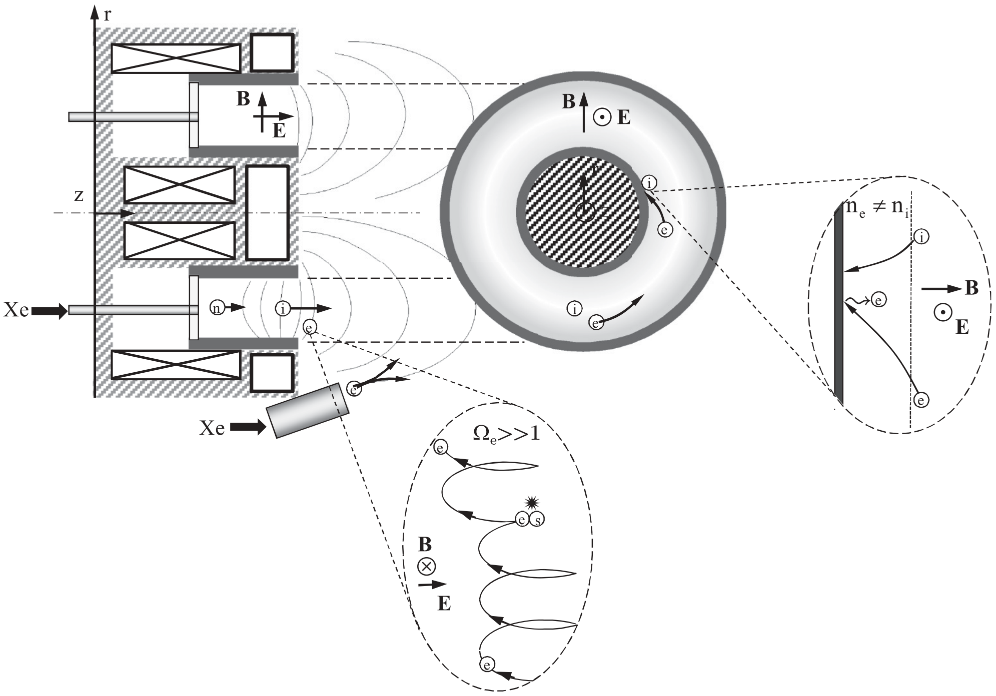

FIG. 1. Schematic of a Hall-effect plasma accelerator (SPT type) showing the basic processes that drive its fundamental principle of operation.

B. Background and overall numerical approach

The high electron Hall parameter established in the thruster chamber leads to the "equipotentialization" and "isothermalization" of the lines of force [14]: Streamlines of the magnetic vector field are, approximately, also lines of constant "thermalized potential" $\phi_T \equiv \phi - T_e \ln(n_e)$ and constant electron temperature T_e. This may allow for a computational simplification in configurations where the magnetic field lines begin at one side of the thruster channel annulus and end at the opposite side. Specifically, it may be possible to solve for the plasma potential and electron temperature in a (quadrilateral) computational cell that is bounded by two adjacent lines of force rather than one with arbitrary dimensions, and then interpolate the solution onto an arbitrary structured mesh. This simplification formed the basis for the development of a number of 2D computational models of Hall thrusters in existence today, such as HPHall, which uses a set of quasi-1D fluid equations for the electrons and a particle-tracking Boltzmann solver for the heavy species in 2D axisymmetric geometry. The code was developed by Fife in the late 1990s [5].

Recent work has shown that the applied magnetic field may be designed in a way to shield the acceleration channel surfaces (and in turn the magnetic poles) from significant ion bombardment [25]. In such "magnetic shielding" topologies a line of force may begin and end at the same surface rather than traverse the channel annulus. Near these surfaces the above-mentioned discretization approach used in HPHall cannot be used to obtain the solution to the electron equations. Also, near the hollow cathode the electron density can become high enough such that the isothermalization of the lines is no longer preserved. In both these cases a more generalized discretization approach is needed. A main challenge with generalized structured meshes, however, is excessive numerical diffusion caused by the large disparity of the transport coefficients in the parallel and perpendicular directions. This may be avoided by discretizing the equations on a computational mesh that is aligned with the magnetic field.

There are three main distinctive features of Hall2De, the combination of which advances the state of the art on the numerical simulation of Hall thrusters:

(a) Discretization of all conservation laws on a MFAM.

(b) Numerical solution of the conservation equations for the heavy species without invoking discrete-particle methods:

(i) Multiple ion fluids can be included, each being treated as an isothermal, cold (relative to the electrons) fluid accounting for the ion drag forces and ion pressure gradient.

(ii) The evolution of the neutral species is computed using line-of-sight formulations that account for ionization collisions and collisions with walls.

(c) Large computational domain that extends several times the thruster channel length in the axial direction and encompasses the cathode boundary and the thruster axis of symmetry.

The first feature allows for the assessment of plasma and erosion physics in regions with complex magnetic field topologies. In these regions of the thruster where isothermalization and thermalized equipotentialization of the lines of force persist, the main distinction between Hall2De and codes that employ the quasi-1D discretization approach is that, in the latter cases, a computational element is defined by two lines of force and two boundary segments, and the solution is then interpolated onto an arbitrary structured mesh. In Hall2De such computational element is further divided into additional elements using an orthogonal set of lines. The equations are then solved on each one of these additional elements. The main advantage here is the ability to simulate regions of the thruster where surfaces have disrupted the lines of force. The MFAM also allows for the self-consistent simulation of the plasma in the near-anode region. By contrast, in HPHall the self-consistent numerical solution of the conservation laws must be terminated at the magnetic field streamline nearest to the anode boundary. In the region between this streamline and the anode the HPHall solution is determined by extrapolation.

Feature (b) eliminates the inherent statistical fluctuations typically caused by particle-based methods, and (c) allows for the investigation of the large-scale behavior of electrons in the plume while accounting for the cathode boundary conditions (BCs) self-consistently. Due in part to the deviations from the isothermal condition along lines of force, which occur typically near the cathode, the extent of the computational domain downstream of the channel exit plane in solvers that incorporate the quasi-1D discretization approach is limited. Shown in Fig. 2(a) is a schematic of a typical Hall2De computational r-z domain with naming conventions of various thruster components and boundaries to be cited throughout this article. The length and height of the acceleration channel are denoted by L and H, respectively. The figure shows also computed gray-scale contours of the electron number density. We note that in the particular configuration shown in Fig. 2 the cathode is located at the thruster centerline (CL) which renders it 2D axisymmetric. For illustrative purposes, Fig. 2(b) shows a photograph of the corresponding laboratory Hall thruster operating in a vacuum facility.

The conservation equations for all species are solved in a time-split manner. Upon initialization, the plasma laws are solved first followed by those for the neutrals. The plasma solvers proceed with the solution for the ion number density first, then for the ion velocity, electron temperature, and plasma potential at the end.

C. Ions

1. Physics model

Because the treatment of ions, specifically the computational methods employed to determine their evolution inside the acceleration channel, has been wide ranging due largely to the assumptions made on their characteristic collision scales, we outline here our estimates of the relevant characteristic sizes for the ions in some detail. The two characteristic times for relaxation to a fluid, τ_e for electrons and τ_i for ions, are

$$\tau_e = \langle \nu_{ei} \rangle^{-1} = \frac{3(2\pi)^{3/2}\varepsilon_0^2\sqrt{m_e}\,(k_B T_e)^{3/2}}{n_i Z^2 q_e^4 \ln\Lambda},$$

$$\tau_i = \langle \nu_{ii} \rangle^{-1} = \frac{12\pi^{3/2}\varepsilon_0^2\sqrt{m_i}\,(k_B T_i)^{3/2}}{n_i Z^4 q_e^4 \ln\Lambda} \tag{4}$$

$$\approx \left(\frac{2m_i}{m_e}\right)^{1/2}\left(\frac{T_i}{T_e}\right)^{3/2}\frac{\tau_e}{Z^2},$$

(with temperature expressed in K). In the remainder of this article, our convention will exclude the brackets from mean values of the collision frequency, that is $\nu \equiv \langle \nu \rangle$. In Eq. (4) T is the temperature, Z is the charge state, k_B is Boltzmann's constant, ε_0 is the permittivity in vacuum, and $\ln\Lambda$ is the Coulomb logarithm. When $T_i \leqslant T_e$ the (Spitzer) thermal equilibration time between slow-moving singly charged ions and electrons may be approximated by

$$\tau_{ei}^T \approx \frac{m_i}{2m_e}\tau_e. \tag{5}$$

Using representative values for a typical laboratory Hall thruster operating at 6 kW [26] the ion transit time $\tau_u = L/u_i$ for a drift velocity u_i can range approximately from $(0.03\text{ m})/(2 \times 10^4\text{ m/s}) = 1.5\,\mu\text{s}$ for those ions that are accelerated downstream of the channel to $(0.01\text{ m})/(5 \times 10^2\text{ m/s}) = 10\,\mu\text{s}$ for those generated near the anode region and lost to the walls. For comparison, the thermal equilibration time between electrons and ions ranges 0.03–0.5 s inside the channel which implies that the ions remain "cold" relative to the electrons. The (thermal) mean free path (mfp) for ion-ion collisions $\lambda_{ii} = u_{Ti}\tau_i$, with $u_{Ti} = (2k_B T_i/m_i)^{1/2}$ being the ion thermal speed, is plotted in Fig. 3(a) along the middle of the acceleration channel in two different Hall thrusters for various values of the ion temperature. It is noted that although a case of 5000 K ions has been plotted it is an extreme case since the channel walls typically do not exceed 1000 K. It will be shown later that

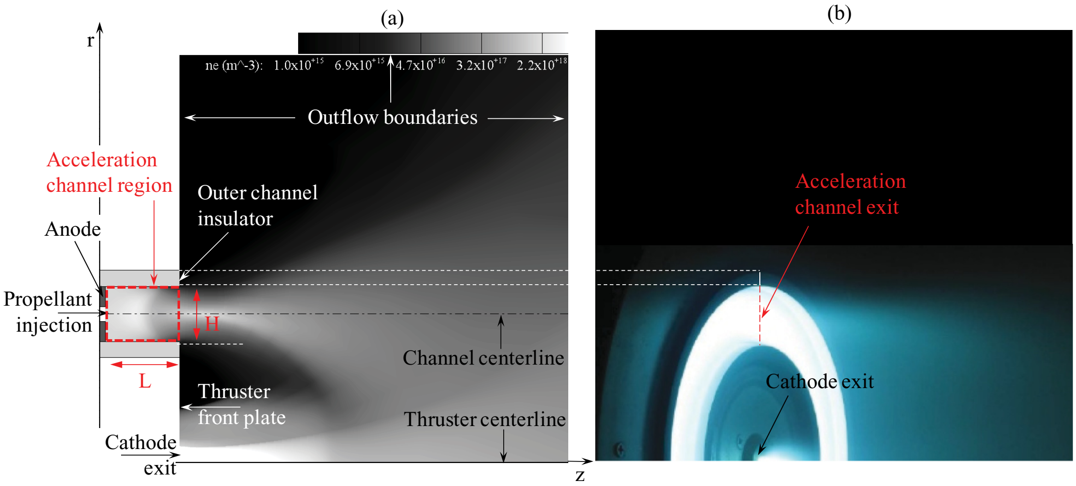

FIG. 2. (Color online) (a) Typical computational domain of a Hall thruster showing naming conventions for various thruster components and boundaries to be cited throughout this paper. (b) Photograph of a laboratory Hall thruster operating in a vacuum facility.

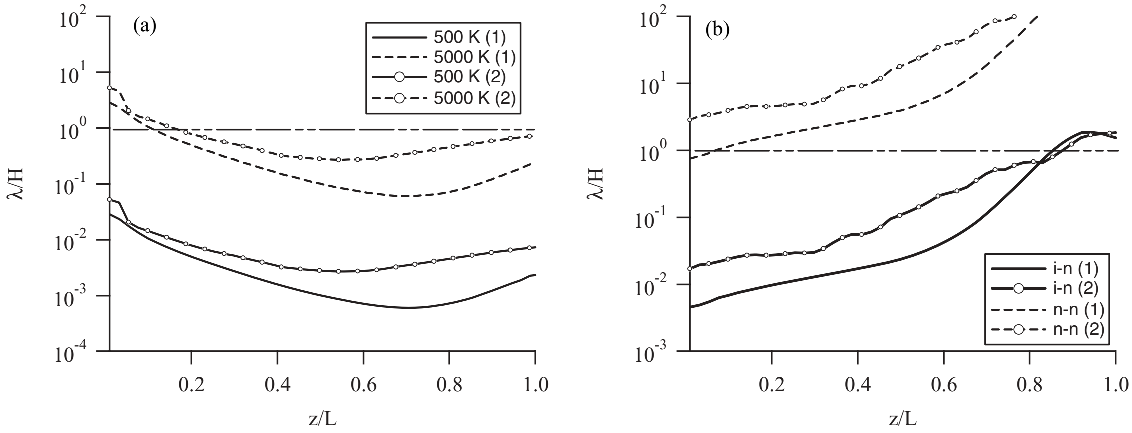

FIG. 3. Ratio of mfp (λ) for collisions over the channel height H at the middle of the acceleration channel in two different thrusters, a 6-kW laboratory thruster (1) and a SPT (2). (a) Ion-ion Coulomb collisions for different values of the ion temperature. (b) Ion-neutral collisions that lead to the exchange of charge (assuming a constant cross section of 50 Å) and neutral-neutral collisions.

the ion density may in fact be substantially higher in the anode region than the values predicted by these simulations, which suggests even smaller collision mfps for ions in this region than those plotted in Fig. 3(a). Also, laser-induced fluorescence measurements of Xe$^+$ inside this Hall thruster have shown that ions follow very closely the equilibrium distribution function [27], which further strengthens the continuum assumption for the ions in this region.

Depicted in Fig. 3(b) is the charge-exchange collision mfp for ions colliding with atoms of number density n_n as estimated by $\lambda_{\mathrm{in}} = (\sigma_{\mathrm{in}} n_n)^{-1}$. The mfp is plotted for two values of the ion-neutral charge-exchange cross section σ_{in}, 50 Å^2 and 100 Å^2. Based on the measurements of Miller *et al.* [28], the two values cover the range of typical ion energies attained in the acceleration channel, <1 eV to 300 eV, with the highest value of the cross section representing the lowest energy ions. For comparison, the characteristic mfp for self-collisions between neutrals $\lambda_{nn} = (\pi n_n D^2 \sqrt{2})^{-1}$ is also plotted in Fig. 3(b) using a mean atomic diameter for xenon of $D = 2.6$ Å. It is noted that the addition of charge-exchange collisions can become increasingly important in the anode region since the electric force can be negligibly small there [29].

Based on the estimates in Fig. 3 the model adopted in Hall2De treats ions as a fluid and includes charge-exchange collisions as a contribution to the (elastic) friction or "drag" force in the fluid momentum equation. The ion temperature is specified; thus an ion energy equation is not solved. Neutrals are assumed to undergo no momentum-exchange collisions with other heavy species. As it will be described later however, collisions of neutrals that lead to loss of electron(s) and collisions with walls are included. The approach for the neutrals is described in Sec. II E. In this section we describe the conservation laws and numerical approach for the ions. Although all equations will be presented for a single ion fluid that accounts for multiple charge states, Hall2De may in fact account up to four distinct ion fluids. This multifluid capability was implemented in recognition of the disparate equilibration times that ions may possess, especially in the near-plume and cathode regions of the thruster. Such disparity can lead to ion populations with displaced Maxwellian distribution functions relative to each other in which case multiple ion conservation equations must be solved. All simulation results presented in this article have been performed for a single ion fluid.

The formulations that lead to the ion momentum conservation law begin with Boltzmann's equation for the distribution function of ions $f_{\mathrm{i}}(\mathrm{t},\mathbf{r},\mathbf{v})$:

$$\frac{\partial f_i}{\partial t} + \mathbf{v} \cdot \nabla_{\mathbf{r}} f_i + \mathbf{F}_i \cdot \nabla_{\mathbf{v}} f_i = (\dot{f}_i)_c, \tag{6}$$

where $\mathbf{F}_i$ is the total specific force on the ions containing the electric and Lorentz forces and t is time. The term on the right expresses the rate of change of the distribution function as a result of collisions between ions and species s and, in general, it may be composed of both elastic and inelastic components. By taking the product of Eq. (6) with the ion momentum $m_i \mathbf{v}_i$, and integrating over velocity space, one obtains the conservation law for the transport of momentum:

$$\frac{\partial}{\partial t}(nm\langle \mathbf{v}\rangle)_i + \nabla_r \cdot (nm\langle \mathbf{vv}\rangle)_i - n_i m_i \langle (\mathbf{F}\cdot\nabla_{\mathbf{v}})\mathbf{v}\rangle_i$$
$$= \int m_i \mathbf{v} (\dot{f}_i)_c d\mathbf{v}, \tag{7}$$

where $\mathbf{v}$ is the particle velocity with respect to the laboratory frame of reference, $\mathbf{u} \equiv \langle \mathrm{v}\rangle = n^{-1}\int \mathbf{v} f d\mathbf{v}$ is the mean particle velocity, and $\mathbf{c} \equiv \mathbf{v} - \mathbf{u}$ is the particle thermal velocity. The momentum conservation law for ions may therefore be expressed in conservative form as follows:

$$\frac{\partial}{\partial t}(nm\mathbf{u})_i + \nabla \cdot (nm\mathbf{uu})_i = q_i n_i \mathbf{E} - \nabla p_i + \mathbf{R}_i, \tag{8}$$

where we have neglected the viscous terms in the pressure tensor ($\mathbf{p}_{\mathrm{i}} \equiv nm\langle \mathbf{cc}\rangle$) and have assumed that $\mathbf{p}_i = p_i \mathrm{I}$ with I being the delta tensor. Because the magnetic induction field in Hall thrusters is static the curl-free condition for the electric $\mathbf{E} = -\nabla\phi$ may be assumed. The drag force density $\mathbf{R}_i$, defined in terms of the collision term on the right in Eq. (7), may be separated into two parts to distinguish the momentum exchange between species by elastic collisions from that by inelastic collisions:

$$\mathbf{R}_i = \int m_i \mathbf{v}(\dot{f}_i)_c d\mathbf{v}\Big|_{\text{elastic}} + \int m_i \mathbf{v}(\dot{f}_i)_c d\mathbf{v}\Big|_{\text{inelastic}}. \qquad (9)$$

Equation (8) may be combined with the equation of ion continuity,

$$\frac{\partial (nm)_i}{\partial t} + \nabla \cdot (nm\langle \mathbf{v}\rangle)_i = \int m_i (\dot{f}_i)_c d\mathbf{v}, \quad = m_i \dot{n}, \qquad (10)$$

to yield the momentum equation in nonconservative form,

$$n_i m_i \frac{D\mathbf{u}_i}{Dt} \approx q_i n_i \mathbf{E} - \sum_{s\neq i} n_i m_i \nu_{\text{is}} (\mathbf{u}_i - \mathbf{u}_s) - \nabla p_i + \mathbf{\Psi}_i . \qquad (11)$$

In Eq. (10) $\dot{n}$ represents the ion production rate. Since the dynamics of the direct and inverse [30] elastic collisions are the same, we have approximated in Eq. (11) the elastic term for collisions with species s in terms of a mean collision frequency ν_{is} between ions and other species s:

$$\int m_i \mathbf{v}(\dot{f}_i)_c d\mathbf{v}\Big|_{\text{elastic}} \approx -\sum_{s\neq i} n_i m_i \nu_{\text{is}} (\mathbf{u}_i - \mathbf{u}_s). \qquad (12)$$

The elastic drag force for a given population of ions accounts for collisions with neutrals as well as Coulomb collisions with ions of different charge states Z. The term $\mathbf{\Psi}_i$ includes all the inelastic contributions to the transport of ion momentum:

$$\mathbf{\Psi}_i \equiv \int m_i \mathbf{v}(\dot{f}_i)_c d\mathbf{v} - m_i \mathbf{u}_i \dot{n}. \qquad (13)$$

It is noted that there are two terms in $\mathbf{\Psi}_i$ which are mathematically distinct. The first appears as a direct consequence of taking the first moment of Eq. (6) to obtain the conservative form of the momentum equation (8). The second term appears because Eqs. (8) and (10) were combined to obtain the nonconservative form of the momentum equation (11). For a quasineutral plasma with only singly charged ions and no recombination, $\mathbf{\Psi}_i$ takes the simple form

$$\mathbf{\Psi}_i = -m_i \dot{n} (\mathbf{u}_i - \mathbf{u}_n). \qquad (14)$$

Quasineutrality is assumed in all formulations presented herein except in those involving sheath BCs. The following ion-production reactions are included:

$$\begin{gathered} e^- + \text{Xe} \rightarrow 2e^- + \text{Xe}^+, \quad e^- + \text{Xe} \rightarrow 3e^- + \text{Xe}^{++}, \\ e^- + \text{Xe} \rightarrow 4e^- + \text{Xe}^{+++}, \quad e^- + \text{Xe}^+ \rightarrow 2e^- + \text{Xe}^{++}, \\ e^- + \text{Xe}^+ \rightarrow 3e^- + \text{Xe}^{+++}, \quad e^- + \text{Xe}^{++} \rightarrow 2e^- + \text{Xe}^{+++}, \\ \text{Xe} + \text{Xe}^+ \rightarrow \text{Xe}^+ + \text{Xe}, \quad \text{Xe} + \text{Xe}^{++} \rightarrow \text{Xe}^{++} + \text{Xe}. \end{gathered} \qquad (15)$$

The ion conservation laws are closed with conditions specified at all boundaries in Fig. 2. At electrical insulators, namely the outer and inner channel walls and the thruster front plate in Fig. 2, the hydrodynamic Bohm criterion $u_i \geqslant (k_B T_e/m_i)^{1/2}$ is imposed for the normal velocity component of ions exiting the physical domain (i.e., at entry into the sheath). The condition assumes cold monoenergetic ions and Bolzmann-distributed electrons in the sheath, and fully absorbing walls. This is a limiting condition when the ion flow normal velocity is less than the ion acoustic speed, and does not take into account contributions of low-energy ions in the ion velocity distribution function [31]. When the normal velocity exceeds the ion acoustic speed *it* is used as the value at the boundary. At the anode, the BC for ions is implemented in a way that ensures a continuous transition from the Bohm condition for the ion velocity to zero velocity as the sheath evolves from ion attracting to ion repelling. The model is based on the formulations of Andrews and Varey [32] (see also [33] for numerical implementation). Reflection boundary conditions are set at the thruster CL (axis of symmetry). At the outflow boundaries the ions are allowed to flow out of the system freely (gradients of the two velocity components are set to zero). The ion flux is specified at the cathode boundary based on independent simulations of the hollow cathode plasma (e.g., see [34]).

2. Numerical approach

Equation (11) is solved using a centered upwind scheme for the velocity field at the vertices of the MFAM. Referring to the filled-circle vertex in Fig. 4, since the simulation domain is composed of quadrilateral computational cells of arbitrary shape the scheme accounts for the surrounding eight vertices (open circles) to determine the upwind direction. Because all the conservation laws in Hall2De are discretized using finite-volume differencing, scalar variables S are computed at the cell centers (filled squares) whereas scalar-gradient and drag force vectors are computed at the cell faces and vertices respectively, as shown in Fig. 4(b).

Specifically, Eq. (11) may be written in the following general form:

$$\frac{\partial \mathbf{u}}{\partial t} + (\mathbf{u}\cdot\nabla)\,\mathbf{u} = \mathbf{G}\,(S) + \tilde{\mathbf{R}}\,(\mathbf{u})\,, \qquad (16)$$

where $\mathbf{G}$ represents the scalar-gradient specific forces and is a function of scalar S. $\tilde{\mathbf{R}}$ is the drag specific force and depends linearly on the velocity $\mathbf{u}$. It is therefore evaluated at the vertices. In general, $\tilde{\mathbf{R}}$ is also a function of the collision frequency, which we approximate at the vertices by bilinear interpolation of the surrounding cell-centered values [Fig. 4(b)]. For illustrative purposes we refer to the 1D stencil in Fig. 5 with an equal spatial increment Δx between vertices

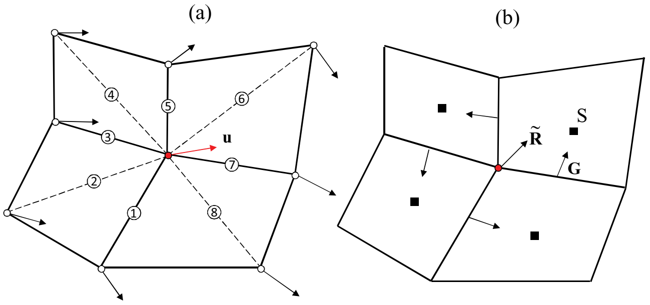

FIG. 4. (Color online) Schematic of a set of four computational cells showing centering of velocities and forces for the solution of the ion momentum equation. The velocity field at the vertices is solved for using an upwind scheme that takes into account the contributions from a maximum of eight surrounding vertices (a). Scalars are defined at cell centers and forces are defined at vertices and cell faces (b).

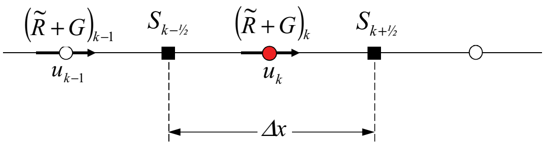

FIG. 5. (Color online) Location of velocities, scalars, and forces on a 1D stencil.

and cell centers, to express the discretized form of Eq. (16) as follows:

$$\frac{u_k^{t+\Delta t}-u_k^t}{\Delta t}+\frac{\left(u_k^t+u_{k-1}^t\right)\left(u_k^t-u_{k-1}^t\right)}{2\Delta x} = \frac{1}{2}\left[(G_\varphi)_k^t+(G_\varphi)_{k-1}^t\right]+(G_p)_k^t+\tilde{R}\left(u_k^t\right), \qquad (17)$$

where $x = k\Delta x$, $k = 0,1,\ldots,N$. The scalar-gradient force is approximated by

$$G_k^t = \frac{S_{k+\frac{1}{2}}^t - S_{k-\frac{1}{2}}^t}{\Delta x}. \qquad (18)$$

In Eq. (17) we have expressed separately the plasma potential and ion pressure gradient forces G_ϕ and G_p to note that, due to its dominance on the acceleration of ions, we implement second-order spatial accuracy in G_ϕ; all remaining terms are first-order accurate. The continuity (10) and momentum (11) equations are advanced explicitly with first-order accuracy in time to yield at $t+\Delta t$ the ion number density and velocity field, respectively.

D. Electrons

1. Physics model

The electron momentum equation in the absence of the viscous terms is given by

$$n_e m_e \frac{D\mathbf{u}_e}{Dt} = -q_e n_e\left(\mathbf{E}+\mathbf{u}_e\times\mathbf{B}\right)-\nabla p_e+\mathbf{R}_e, \qquad (19)$$

where we have expressed the electron pressure as $\mathbf{p}_e = p_e\mathrm{I}$. As in the case for ions, the friction force $\mathbf{R}_e/n_e$ for electrons is related to the integral of the collision term in the evolution equation for the electron distribution function. For the case of a near- (or "quasi-") Maxwellian distribution function in an anisotropic, classical plasma (i.e., with no random fluctuations in the fields), and assuming $\mathbf{u}_e \gg \mathbf{u}_n$, $\mathbf{R}_e$ may be approximated as follows:

$$\mathbf{R}_e \approx -n_e m_e\left[\sum_i \nu_{ei}\left(\mathbf{u}_e-\mathbf{u}_i\right)+\nu_{en}\mathbf{u}_e\right] = q_e^{-1}m_e\left(\bar{\nu}_{ei}+\nu_{en}\right)\mathbf{j}_e+\left(q_e Z^*\right)^{-1}m_e\bar{\nu}_{ei}\sum_i Z\mathbf{j}_i, \qquad (20)$$

with the electron and ion current densities given by $\mathbf{j}_e = -q_e n_e\mathbf{u}_e$ and $\mathbf{j}_i = q_i n_i\mathbf{u}_i = q_e Z n_i\mathbf{u}_i$, respectively. The total electron-ion (e-i) collision frequency is

$$\bar{\nu}_{ei} = \frac{n_e Z^* q_e^4 \ln\Lambda}{3\left(2\pi\right)^{3/2}\varepsilon_0{}^2\sqrt{m_e}\left(k_B T_e\right)^{3/2}}, \quad Z^* \equiv n_e^{-1}\sum_i n_i Z^2. \qquad (21)$$

Unless otherwise noted all references to "e-i collision frequency" in the remainder of this article shall imply the definition in Eq. (21). It has also been proposed that the transport of electrons in Hall thrusters is enhanced in a nonclassical manner, specifically by plasma turbulence [35,36] and/or collisions with the channel walls [14,37]. In numerical simulations of Hall thrusters these additional transport mechanisms are accounted for through the addition of nonclassical collision frequency models the physics of which are beyond the scope of this article. For simplicity but without loss of generality we shall represent all nonclassical contributions to the total electron collision frequency as ν_α.

If the electron inertia can be neglected then one obtains the vector form of Ohm's law:

$$\mathbf{E} = \eta\mathbf{j}_e + \eta\Omega_e\mathbf{j}_e\times\hat{\boldsymbol{\beta}} - \frac{\nabla p_e}{q_e n_e} + \eta_{ei}\bar{\mathbf{j}}_i, \qquad (22)$$

where

$$\eta = \frac{m_e\nu_e}{q_e{}^2 n_e}, \quad \eta_{ei} = \frac{m_e\bar{\nu}_{ei}}{q_e{}^2 n_e}, \quad \bar{\mathbf{j}}_i = \frac{1}{Z^*}\sum_i Z\mathbf{j}_i. \qquad (23)$$

The total collision frequency of electrons has been expressed as the sum of the individual frequencies, $\nu_e \equiv \bar{\nu}_{ei} + \nu_{en} + \nu_\alpha$. In the frame of reference of the magnetic field, with $\parallel$ and $\perp$ denoting parallel and perpendicular components respectively, the components of Eq. (22) may be written as

$$E_{||} = \eta j_{e||} - \frac{\nabla_{||}p_e}{q_e n_e} + \eta_{ei}\bar{j}_{i||}, \qquad (24a)$$

$$E_\perp = \eta\left(1+\Omega_e{}^2\right)j_{e\perp} - \frac{\nabla_\perp p_e}{q_e n_e} + \eta_{ei}\bar{j}_{i\perp}. \qquad (24b)$$

Equations (24) imply that there are sufficient collisions to sustain the equilibrium distribution function for the electrons in each direction relative to the magnetic field. Estimates of the minimum collision mfp for electrons inside the acceleration channel suggest that the collisionality of the species parallel to the magnetic field may be insufficient to warrant the continuum form of Ohm's law as expressed by the expression on the left of Eq. (24). Our simulations confirm, however, that the resistive terms in the parallel direction are negligible compared to the remaining terms. Then effectively we have $E_{||} \approx \nabla_{||}p_e/q_e n_e$, which yields the expected dependence of the plasma potential on the electron temperature and number density in the parallel direction.

The electron energy conservation law is solved for the electron temperature (expressed in eV) and is given by

$$\frac{3}{2}q_e n_e\frac{\partial T_e}{\partial t} = \mathbf{E}\cdot\mathbf{j}_e + \nabla\cdot\left(\frac{5}{2}T_e\mathbf{j}_e - \mathbf{Q}_e\right) - \frac{3}{2}T_e\nabla\cdot\mathbf{j}_e - \sum_s\Phi_s + Q_e^T, \qquad (25)$$

where, as in the case of the resistive terms, the thermal conduction heat-flux tensor $\mathbf{Q}_e$ is discretized on the MFAM in terms of its parallel and perpendicular components: $Q_{e||} = -\kappa_{e||}\nabla_{||}T_e$ and $Q_{e\perp} = -\kappa_{e\perp}\nabla_\perp T_e$. The same arguments that were made regarding the insignificance of the resistive terms in the parallel direction apply also to $\mathrm{Q}_{e||}$, which implies that the isothermalization of the lines is preserved. The last term on the right of Eq. (25) represents the energy exchange per unit time between electrons and the heavy species [38] due to deviations from thermal equilibrium, and is proportional to $n_e(m_e/m)\nu_{ei}(T_e - T_i)$ for ions and $n_e(m_e/m)\nu_{en}(T_e - T_n)$ for neutrals. In Hall thrusters this term is usually a small contribution to the total electron energy. Inelastic energy losses associated with collisions of electrons with species s that produce species s' ($s \to s'$) are accounted for by

$$\sum_s \Phi_s = q_e(\phi' - 1)\,(\dot{n}\zeta)_{n\to i} + q_e \sum_{s\to s'} \left[(\dot{n}\zeta)_{s\to s'} + \frac{3}{2}\,(Z_{s'} - Z_s)\,T_e \right], \qquad (26)$$

where

$$\varphi' \equiv \frac{\varphi}{\zeta_{n\to i}} = A_0 e^{(A_1\zeta_{n\to i}/T_e)} + A_2, \quad \dot{n}_{s\to s'} \equiv n_e n_s \langle \sigma \mathbf{v}_e \rangle_{s\to s'}. \qquad (27)$$

Electron excitation losses are included in the first term of Eq. (26) and account only for ground-state transitions. In Eq. (27) φ represents the nondimensional excitation energy loss, $\langle \sigma \mathbf{v}_e \rangle$ is the impact ionization rate, and ζ is the ionization potential. The excitation loss rate is based on a fit to a solution derived by Dugan and Sovie [39] with coefficients $A_0 = 0.6$, $A_1 = 0.304$, and $A_2 = 1$.

The plasma potential is determined by solving the equation of current conservation:

$$\nabla \cdot \mathbf{j} = 0, \qquad (28)$$

with the total current density given by $\mathbf{j} = \mathbf{j}_e + \mathbf{j}_i$. Equations (24) are expressed in terms of the electron current density and are then substituted into Eq. (28) which is solved in two directions, parallel and perpendicular to the magnetic field. The numerical approach for its solution is described in the next section.

The equations for the electrons are closed with BCs at all surfaces in Fig. 2. At the anode, sheath BCs are implemented for the electron and ion current densities normal to the boundary. The ion current density is prescribed based on the Bohm criterion (Sec. II C 1). The electron current density is given by

$$\mathbf{j}_e \cdot \hat{\mathbf{n}} = \begin{cases} -j_{Te} e^{-q_e\Delta\varphi/k_B T_e}, & \Delta\varphi > 0, \\ -j_{Te}, & \Delta\varphi \leqslant 0, \end{cases} \qquad (29)$$

and the convective heat flux is

$$(\mathbf{j}_e T_e) \cdot \hat{\mathbf{n}} = \mathbf{j}_e \cdot \hat{\mathbf{n}}\,(2T_e + \Delta\varphi)\,, \qquad (30)$$

where $\Delta\phi = \phi - V_A$ is the potential drop across the sheath at the boundary and the electron thermal flux is $j_{T_e} = n_e\,(8k_B T_e/\pi m_e)^{1/2}/4$. Typically in Hall thrusters the sheath at the anode is electron repelling ($\Delta\phi > 0$). Equations (29) and (30) are evaluated using the plasma potential value ϕ at the center of the computational cell that is located adjacent to the wall boundary, where $\hat{\mathbf{n}}$ is the unit vector normal to the boundary. The conductive heat flux at the sheath is set to zero, $\mathbf{q}_e \cdot \hat{\mathbf{n}} = 0$. At the cathode boundary the conditions for the electrons are specified directly for the neutral particle flux, plasma potential, and electron temperature. All such conditions are guided by independent numerical simulations of the partially ionized gas generated by the hollow cathode (e.g., see [34]).

For all insulator wall boundaries a zero-current condition is imposed: $\mathbf{j}\cdot\hat{\mathbf{n}} = 0$. The conductive heat flux also is set to zero. To account for the secondary electron emission from these boundaries the convective heat loss [Eq. (30) above] follows the formulations of Hobbs and Wesson (H&W) [40]. Specifically, given the electron temperature and plasma potential at the sheath-plasma edge, $\Delta\phi$ is determined based on the H&W solution to the 1D sheath equations, given the material-dependent secondary electron yield function. Because outflow boundaries are far from the channel exit Dirichlet conditions are implemented for the electron temperature. Based on direct measurements, at a distance that is several times the channel length, the electron temperature varies typically in most Hall thrusters between 1 and 4 eV. For the current density at the plume boundaries the zero-current condition is imposed.

2. *Numerical approach*

The large disparity (more than two orders of magnitude in regions with high values of the magnetic field) that exists in the electron transport equations between the perpendicular and parallel directions requires special treatment. In this section the general approach is outlined using Eq. (28) as the example equation. The plasma potential is solved by combining Eqs. (24) and (28) into one equation. Then, referring to Fig. 6(b), for a single quadrilateral computational cell with volume ΔV, consisting of four faces each identified by index $k = 1,\ldots,4$, and each having surface area ΔA, the divergence theorem leads to the following discretization:

$$\int_V \nabla \cdot \mathbf{j}dV = \oint_A \mathbf{j} \cdot d\mathbf{A} \approx \sum_{k=1}^{4} (\mathbf{j} \cdot \hat{\mathbf{n}}\Delta A)_k. \qquad (31)$$

The current density may be expressed in terms of its components parallel and perpendicular to the magnetic field:

$$\sum_{k=1}^{4} (\mathbf{j} \cdot \hat{\mathbf{n}}\Delta A)_k = \sum_{k=1}^{4} [(\mathbf{j}_{||} + \mathbf{j}_{\perp}) \cdot \hat{\mathbf{n}}\Delta A]_k, \qquad (32)$$

where

$$\mathbf{j}_{||} = (\mathbf{j} \cdot \hat{\boldsymbol{\beta}})\hat{\boldsymbol{\beta}}, \quad \mathbf{j}_{\perp} = -\hat{\boldsymbol{\beta}} \times (\hat{\boldsymbol{\beta}} \times \mathbf{j}). \qquad (33)$$

By using Eq. (24) to solve for the current density and subsequently substituting into Eq. (32), the dot product in Eq. (31) at cell face k may be expressed as

$$\mathbf{j}_k^{t+\Delta t} \cdot \hat{\mathbf{n}}_k = \left(\mathbf{E}_k^{t+\Delta t} + \boldsymbol{\varepsilon}_k^t\right) \cdot \frac{\bar{\mathbf{n}}_k^t}{\eta_k^t} \qquad (34)$$

at $t + \Delta t$, where $\bar{\mathbf{n}} \equiv \bar{n}_r\hat{\mathbf{r}} + \bar{n}_z\hat{\mathbf{z}}$. With $\hat{\boldsymbol{\beta}} = \beta_r\hat{\mathbf{r}} + \beta_z\hat{\mathbf{z}}$ the components $\bar{n}_r$ and $\bar{n}_z$ may be simplified on the MFAM as

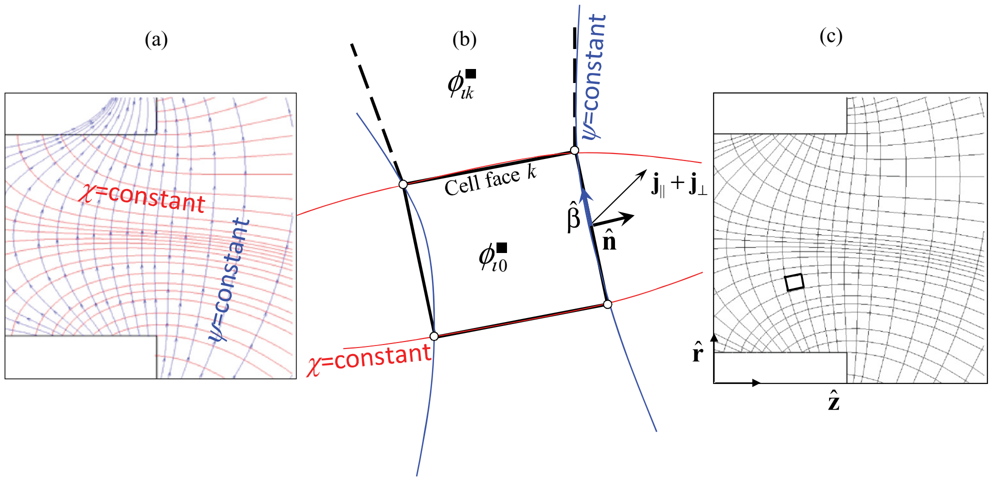

FIG. 6. (Color online) (a) A set of lines of constant stream function ψ (streamlines of the magnetic field) overlaid by lines of constant potential function χ, in the vicinity of the acceleration channel in a typical Hall thruster. (b) Each face of a computational cell in Hall2De is closely aligned with either a χ line or a ψ line. (c) Corresponding MFAM computational mesh.

follows:

$$\text{edge is parallel to }\psi\text{-line}\begin{cases}\bar{n}_r \equiv \beta_r \cancelto{0}{(\beta_r\hat{\mathbf{r}}+\beta_z\hat{\mathbf{z}})\cdot\hat{\mathbf{n}}} + \dfrac{\beta_z}{1+\Omega_e^2}\cancelto{1}{(\beta_z\hat{\mathbf{r}}-\beta_r\hat{\mathbf{z}})\cdot\hat{\mathbf{n}}}\\ \bar{n}_z \equiv \beta_z \cancelto{0}{(\beta_r\hat{\mathbf{r}}+\beta_z\hat{\mathbf{z}})\cdot\hat{\mathbf{n}}} - \dfrac{\beta_r}{1+\Omega_e^2}\cancelto{1}{(\beta_z\hat{\mathbf{r}}-\beta_r\hat{\mathbf{z}})\cdot\hat{\mathbf{n}}}\end{cases}$$

$$\text{edge is parallel to }\chi\text{-line}\begin{cases}\bar{n}_r \equiv \beta_r \cancelto{1}{(\beta_r\hat{\mathbf{r}}+\beta_z\hat{\mathbf{z}})\cdot\hat{\mathbf{n}}} + \dfrac{\beta_z}{1+\Omega_e^2}\cancelto{0}{(\beta_z\hat{\mathbf{r}}-\beta_r\hat{\mathbf{z}})\cdot\hat{\mathbf{n}}}\\ \bar{n}_z \equiv \beta_z \cancelto{1}{(\beta_r\hat{\mathbf{r}}+\beta_z\hat{\mathbf{z}})\cdot\hat{\mathbf{n}}} - \dfrac{\beta_r}{1+\Omega_e^2}\cancelto{0}{(\beta_z\hat{\mathbf{r}}-\beta_r\hat{\mathbf{z}})\cdot\hat{\mathbf{n}}}\end{cases} \tag{35}$$

In Eq. (34) the electric field is replaced by the plasma potential gradient and the remaining terms involving the electron pressure and the ion current terms are included in the term ε. Numerical diffusion due to the disparity between the terms with and without ω_e is reduced by assuming that cell faces are exactly either parallel or perpendicular to the magnetic field lines. The accuracy of the solution is then dependent upon the extent of the spatial deviations of the mesh from the true lines of constant potential and stream functions χ and ψ. Here, χ and ψ are the commonly used set of conjugate harmonic functions satisfying the Cauchy-Riemann conditions for the radial and axial components of the magnetic field. A set of such lines in the vicinity of the acceleration channel of a typical Hall thruster are shown in Fig. 6(a). The corresponding MFAM for this thruster is shown in Fig. 6(c).

The treatment of the sheath BCs requires some discussion. Referring to Fig. 6(b), if $k = b$ is a boundary face with conditions given by Eq. (29) then Eq. (31) may be expanded as follows:

$$\sum_{k\neq b}^{4} C_k^t\left(\varphi_{\iota 0}^{t+\Delta t}-\varphi_{\iota k}^{t+\Delta t}\right) + \sum_{k\neq b}^{4} c_k^t \boldsymbol{\varepsilon}_k^t\cdot\bar{\mathbf{n}}_k^t + \Delta A_b\left(\mathbf{j}_{eb}^{t+\Delta t}+\mathbf{j}_{ib}^t\right)\cdot\hat{\mathbf{n}}_b = 0, \tag{36}$$

where C and c contain the transport and geometrical coefficients. We note that the electron current density at face b is implicit and nonlinear in ϕ due to the exponential term in Eq. (29). Using a Taylor series expansion, for an electron-repelling sheath the BC may be linearized as follows:

$$\begin{aligned}(\mathbf{j}_e\cdot\hat{\mathbf{n}})_b^{t+\Delta t} &= (j_{Te})_b^t \exp\left(-\frac{q_e\Delta\phi_b^{t+\Delta t}}{k_B T_{eb}^t}\right)\\ &\approx (\mathbf{j}_e\cdot\hat{\mathbf{n}})_b^t\left[1-\frac{q_e}{k_B}\left(\frac{\phi^{t+\Delta t}-\phi^t}{T_e^t}\right)_{\iota 0}\right].\end{aligned} \tag{37}$$

As implied by Eq. (34), the current conservation law is solved implicitly for the plasma potential whereas all other terms are explicit.

The equation for the electron temperature is also solved in a semi-implicit fashion. The thermal conduction term is implicit whereas all other terms are evaluated at the previous time step:

$$\begin{aligned}&\frac{3}{2}q_e n_e^t\frac{T_e^{t+\Delta t}-T_e^t}{\Delta t}-\nabla\cdot\left(\boldsymbol{\kappa}_e^t\cdot\nabla T_e^{t+\Delta t}\right)\\ &\approx\left[\mathbf{E}\cdot\mathbf{j}_e+\nabla\cdot\left(\frac{5}{2}T_e\mathbf{j}_e\right)-\frac{3}{2}T_e\nabla\cdot\mathbf{j}_e-\sum_s\Phi_s+Q_e^T\right]^t.\end{aligned} \tag{38}$$

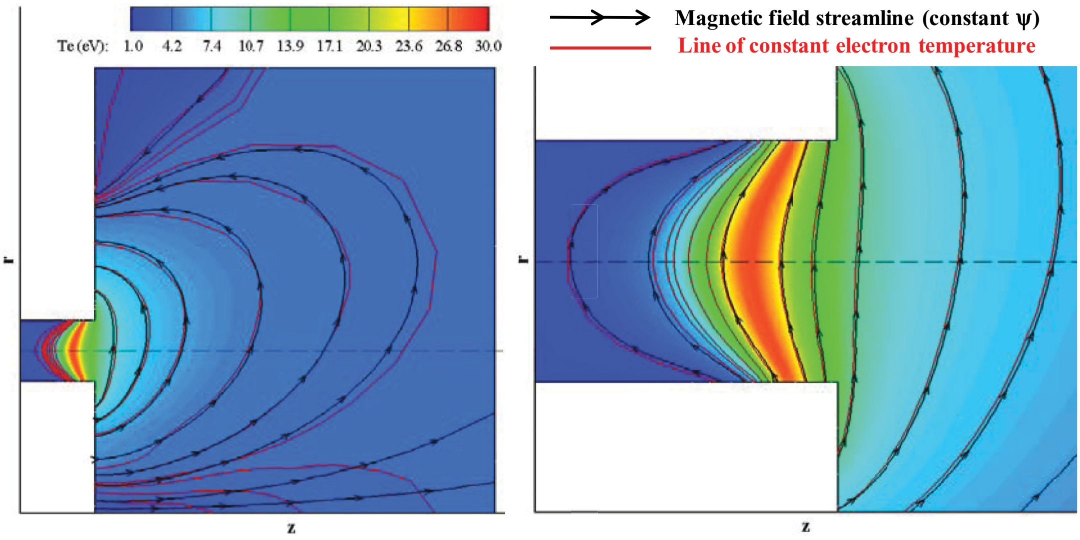

FIG. 7. (Color online) Hall2De preserves the isothermal properties of the lines of force, a well-known feature in Hall thrusters. The plot shows computed electron temperature contours overlaid by selected lines of constant stream function ψ (i.e., streamlines of the magnetic field). The contoured plot for the electron temperature is overlaid by magnetic field streamlines to illustrate their isothermal properties in regions of the thruster where $\Omega_e \gg 1$. Selected T_e contours are illustrated by the solid lines without arrows. To allow for the self-consistent determination of the electron temperature in regions (such as the cathode near-plume) where deviations from isothermal conditions may occur, Hall2De does not specify *a priori* that the electron temperature remains fixed along magnetic field lines.

The solution to all implicit equations in Hall2De is obtained using parallel sparse direct and multirecursive iterative linear solvers (PARDISO). PARDISO is a high-performance, memory efficient package for solving large sparse symmetric and asymmetric linear systems of equations on shared-memory and distributed-memory multiprocessors [41,42]. In Fig. 7 we show computed electron temperature contours in the entire computational region [Fig. 7(a)] and in the vicinity of the acceleration channel [Fig. 7(b)] in a typical Hall thruster. The contours are overlaid by streamlines of the magnetic field to illustrate that in the majority of the computational domain the isothermalization of the lines of force, a well-known feature of conventional Hall thrusters, is preserved. Deviations do occur, however, in the cathode region due to the high collisionality of the plasma there.

E. Atoms

1. *Physics model*

Although collisions that lead to the ionization of an atom can be frequent by comparison to its transit time inside the channel, for most Hall thrusters, collisions between neutrals are rare [see also Fig. 3(b)]. The conservation equation that describes the evolution of the distribution function of the atomic species $f_n(\mathrm{t},\mathbf{r},\mathbf{v})$ is the same as that for ions [Eq. (6)] but with force **F** equal to zero:

$$\frac{\partial f_n}{\partial t} + \mathbf{v}\cdot\nabla_{\mathbf{r}} f_n = (\dot{f}_n)_c. \tag{39}$$

We consider only ionization collisions and approximate the rate of change of the distribution function due to such collisions as

$$(\dot{f}_n)_c = -\nu_{en}^I f_n, \tag{40}$$

where ν_{en}^I is the electron-neutral ionization collision frequency. The number density of neutrals is then determined by integration over the velocity space **v**:

$$n_n(t,\mathbf{r}) = \int_{\mathbf{v}} f_n(t,r,\mathbf{v}')\,d\mathbf{v}'. \tag{41}$$

The algorithm to determine the neutral gas density was developed by Katz and Mikellides and has been described in detail in [22]. Here we only outline the basic concept. The algorithm takes advantage of the long mfp of neutrals to assume that all particles proceed along straight-line, constant-velocity trajectories until they are either ionized, strike a wall, or leave the physical domain. For neutrals emitted from a boundary, $f_n(\mathrm{t},\mathbf{r},\mathbf{v})$ is taken to follow a cosine distribution that remains unchanged except for a scale factor to reflect the loss of neutrals by ionization. The emitted neutrals from any given solid surface include thermally accommodated neutrals from all other surfaces and ions from the plasma that recombined with an electron at the surface. The sources of neutrals in the thruster are gas inlets and solid boundaries. At the anode propellant injection inlet the particle flux is specified based on the operating flow rate of the thruster. At the cathode exit the flux is specified based on independent simulations of the hollow cathode flow through the orifice.

2. *Numerical approach*

A popular numerical method for simulating the flow of particles undergoing rare collisions, such as neutrals in Hall thrusters, is PIC [43] combined with DSMC [44] to account for ionization collisions. An inherent disadvantage of such methods is the numerical noise that is generated due to the particle statistics. The noise may be reduced by including more particles but at the expense of increased computation time, and/or by careful tailoring of the weighting and emission algorithms [10]. The approach followed here aims at eliminating statistical noise. It is based on commonly

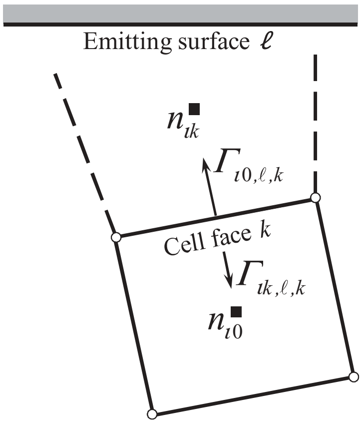

FIG. 8. Definitions of the number densities and particle fluxes for neutrals in a computational cell relative to a neutral-emitting surface.

used methods to model such problems as photon transport in radiation heat transfer.

It is assumed that particles striking a surface are fully accommodated and that the fraction of those particles that is reemitted follows a cosine distribution. Referring to the notation in Fig. 8, Katz and Mikellides [22] showed that integration of Eq. (39) and subsequent discretization yields

$$n^{t+\Delta t}_{\iota 0,\ell} = n^{t}_{\iota 0,\ell} + \Delta t\left[\sum_{k=1}^{4}\frac{\Delta A_k}{\Delta V_{\iota 0}}\left(\Gamma^{t}_{\iota k,\ell,k} - \Gamma^{t}_{\iota 0,\ell,k}\right) - \nu^{t}_{\iota 0} n^{t}_{\iota 0,\ell}\right], \tag{42}$$

where the particle fluxes are given by

$$\Gamma^{t}_{\iota 0,\ell,k} = n^{t}_{\iota 0,\ell} D_{\iota 0,\ell,k}\left(\frac{8k_B T_\ell}{\pi m}\right)^{1/2}. \tag{43}$$

$D_{\iota k,\ell,k}$ is a geometric coefficient that is based on the view factors between face k and surface ℓ. Equation (42) has the form of the fluid continuity equation except for the fact that there are two fluxes at each face k: $\Gamma_{\iota k,\ell,k}$ is associated with gas particles entering computational cell $\iota 0$ from ιk, and $\Gamma_{\iota 0,\ell,k}$ for particles leaving cell $\iota 0$. The corresponding two velocities at each face are proportional to the average molecular speed $(8k_B T/\pi m)^{1/2}$ where the temperature T of the neutrals is equal to that of surface ℓ and its values is specified *a priori*. We note that Eq. (43) implies also that the particle fluxes are upwind fluxes. For clarity on the numerical indices we have dropped the subscripts n and en from the neutral gas density n_n and electron-neutral ionization frequency ν^{I}_{en}. Then, the total neutral number density at the cell center is the contribution from all emitting surfaces ℓ:

$$n^{t+\Delta t}_{\iota 0} = \sum_{\ell} n^{t+\Delta t}_{\iota 0,\ell}. \tag{44}$$

The main approximation in this algorithm is that neutral velocities are independent of time. They are calculated only once using the velocity distribution at the source and by assuming no ionization. This implies also that changes in the velocity field of the neutrals due to charge-exchange collisions are ignored. We found the latter not to have a significant effect on the plasma since the region where it is affected most by charge exchange is near the anode where both ions and neutrals are slow. Because particle trajectories are taken to be straight lines the velocity at any given surface depends then on the view factor

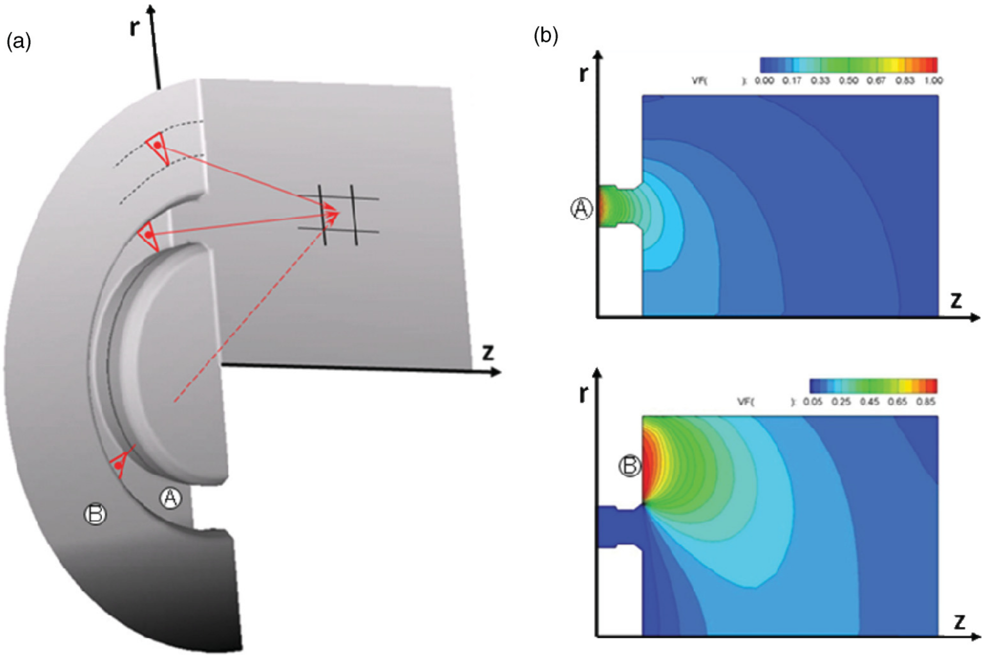

FIG. 9. (Color online) 3D schematic showing the r-z computational domain and portions of the Hall thruster surfaces that contribute neutrals to the domain by emission (a). The emitting surfaces are divided into triangles and the contribution of all triangles is summed to yield the geometrical view factors at the r-z domain (b). Blocked rays do not contribute to the view factors.

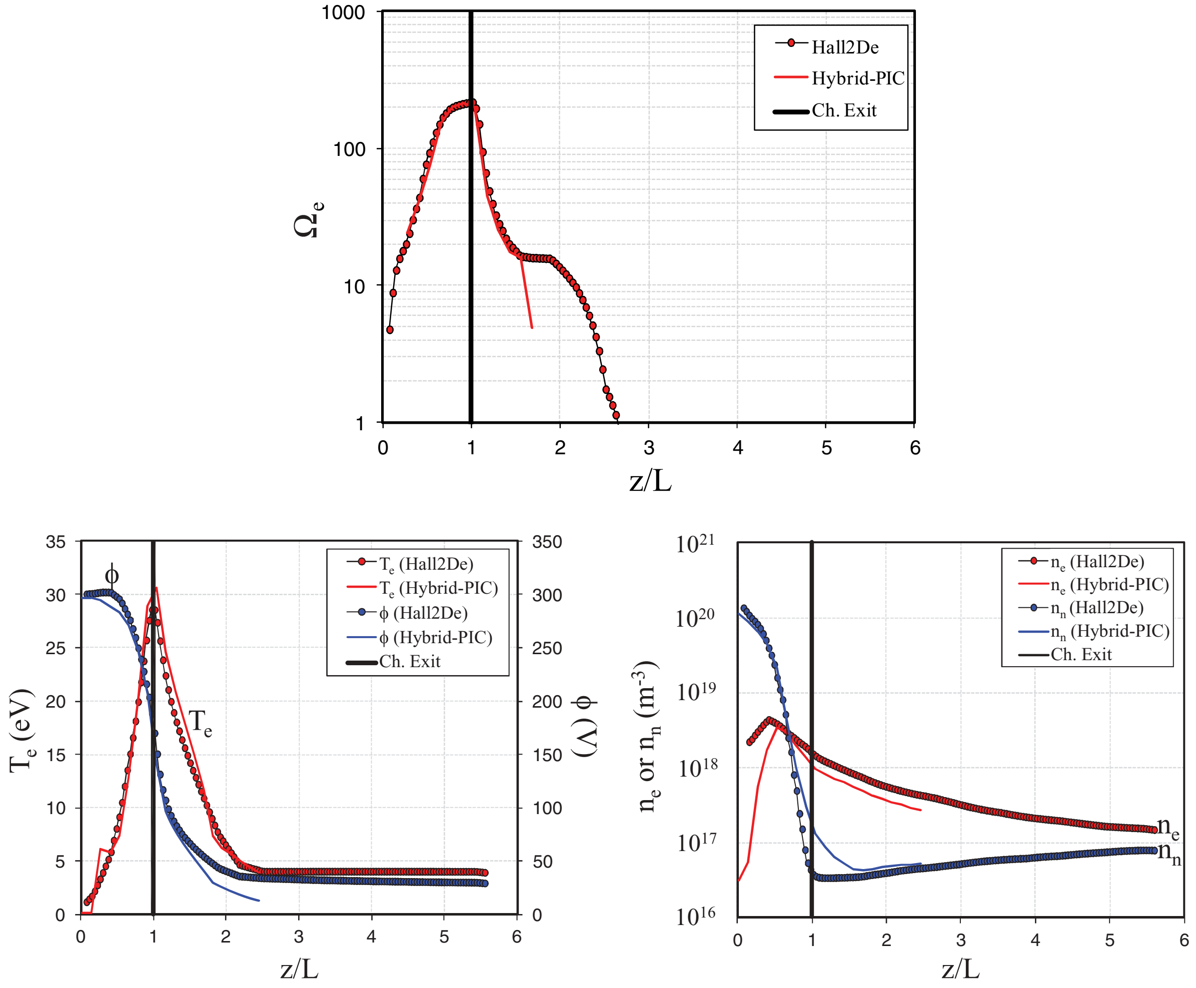

FIG. 10. (Color online) Axial slice plots from the benchmark numerical simulations of a commercial Hall thruster. The plots compare the solution obtained along the channel CL by hybrid-PIC (HPHall) simulations with quasi-1D meshing with that obtained by the MFAM Hall2De.

between that surface and all other surfaces that emit neutrals. Since the basis for computing particle distributions in a region bounded by emission surfaces is the view factors the problem then becomes essentially a problem in geometry. The view factors can be computed at the initialization phase of the simulation, thereby contributing an insignificant amount to the total computation time. The determination of these velocities on a computational mesh with cylindrical geometry proceeds by first generating a surface of revolution for each emitting surface ℓ. The surface is then divided into triangles and for each triangle a ray connects the center of the cell to that of the triangle. If the ray intersects any boundary surface prior to reaching the cell center the ray is considered blocked as shown by the dashed line in Fig. 9. The discrete solid angles needed for the determination of $D_{\iota k,\ell,k}$ are found by summing the view factors of the triangles with unblocked rays. The view factor for each triangle is calculated using the algorithm of Oosterom and Strackee [45]. An example of computed view factors from two surfaces in a typical thruster are shown in Fig. 9(b).

Currently, the algorithm uses approximately ten emitting surfaces. As in the case of PIC where accuracy may be improved by increasing the number of particles, the accuracy of the present algorithm may be improved by increasing the number of the discrete solid angles, i.e., by increasing the number of emitting surfaces ℓ. Regarding our assumption that the speed distribution function of the neutrals does not change by ionization collisions, numerical experiments and comparisons with exact (1D) solutions showed that the accuracy of the algorithm may be improved by dividing the Maxwellian speed distribution into two or more velocity bins [22]. We have found that with three velocity bins the error is less than 20% within six ionization mean free paths. Finally, benchmarking tests demonstrated that because the algorithm does not depend on discrete-particle statistics it eliminates completely statistical noise [22].

III. BENCHMARK NUMERICAL SIMULATIONS AND NEAR-ANODE EFFECTS

We performed a series of Hall2De algorithm tests and comparisons with existing results [24] obtained by HPHall hybrid-PIC simulations of a commercial Hall thruster [23]. A summary of the comparisons is presented in this section. Because nonclassical transport of electrons, arguably occurring in the vicinity of the channel exit, is beyond the scope

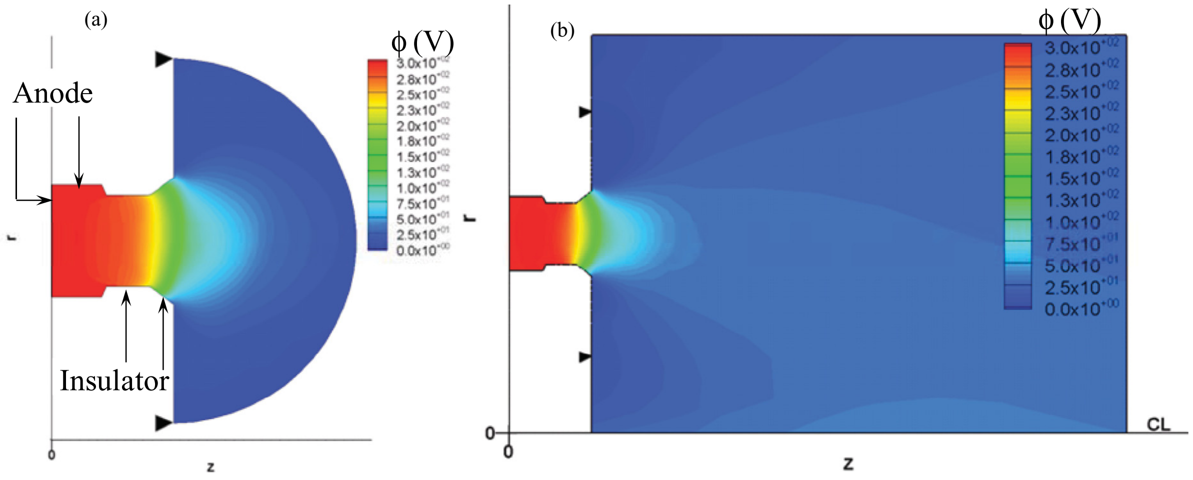

FIG. 11. (Color online) Contour plots from the benchmark numerical simulations of a commercial Hall thruster. The plots compare the solution obtained along the channel CL by hybrid-PIC (HPHall) simulations with quasi-1D meshing (a), with that obtained by the MFAM Hall2De (b). The two filled-triangle symbols point to the maximum radial extent of the HPHall computational region. The electrical boundary types of the channel are also shown. The cathode is located above the upper filled-triangle symbol.

of this article we employed the same collision frequency ν_α in the acceleration channel and near-plume regions as in the hybrid-PIC simulations. This frequency includes the effects of wall collisions.

Comparisons between Hall2De and hybrid-PIC simulations for a variety of computed properties along the channel CL are shown in Fig. 10. Figure 11 depicts 2D contours of the plasma potential. In these comparisons we used Dirichlet BCs for the electron temperature and plasma potential at the anode instead of sheath BCs. Also, excitation losses were excluded at first. Then we repeated the simulations with sheath BCs and excitation losses to illustrate the impact of these physics on the behavior of the near-anode plasma. This is discussed later in the section. Also, the Hall2De results in these simulations were produced using first-order accuracy on the force G_ϕ [Eq. (17)], the neutral gas solver used only one bin for the velocity distribution function, and the ion drag force due to interactions with other heavy species accounted only for charge-exchange collisions with neutrals; Coulomb collisions with ions of different charge states were excluded. Subsequent simulations have shown that although these Hall2De augmentations have a noticeable impact on the plasma solution in the vicinity of the channel exit and plume regions, they affect negligibly the near-anode region.

The Dirichlet BC specified the electron temperature at 1 eV and the plasma potential at 300 V ($= V_A$) to duplicate the HPHall result in this region. It is noted that due to the quasi-1D assumption and associated discretization approach, the HPHall solution near the anode is obtained by extrapolation of the results from a region where the governing equations are solved self-consistently. The two regions—one with extrapolated solution and one with self-consistent solution—are joined along a magnetic field line that serves, effectively, as the anode boundary in HPHall. This is a good approximation in thrusters

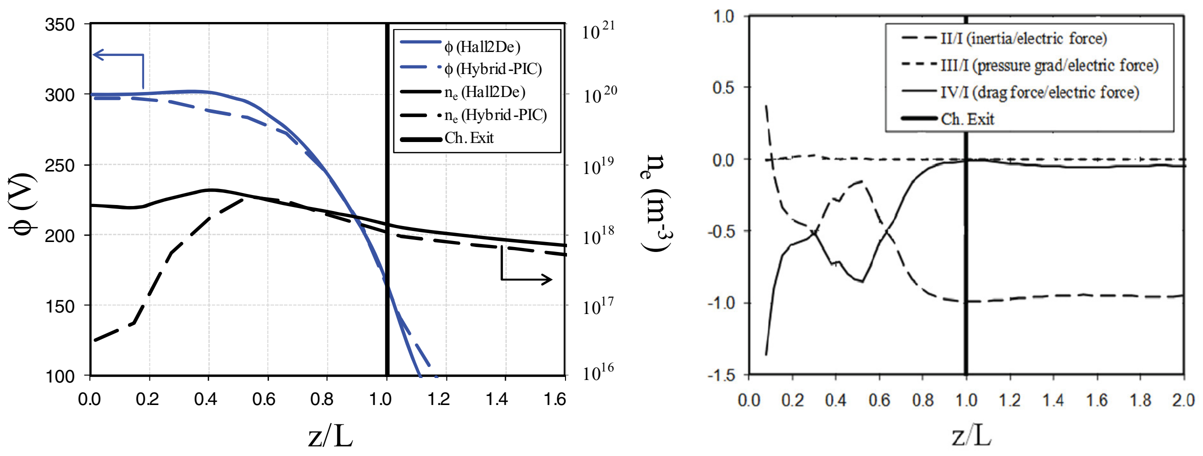

FIG. 12. (Color online) Comparison of terms in the ion momentum conservation law for singly charged ions [Eq. (45)] along the channel CL. The profiles on the right identify the anode or "ion-diffusion" region ($z/L \lesssim 0.3$), the ionization region ($0.3 < z/L < 0.6$), and the ion-acceleration region ($z/L > 0.6$).

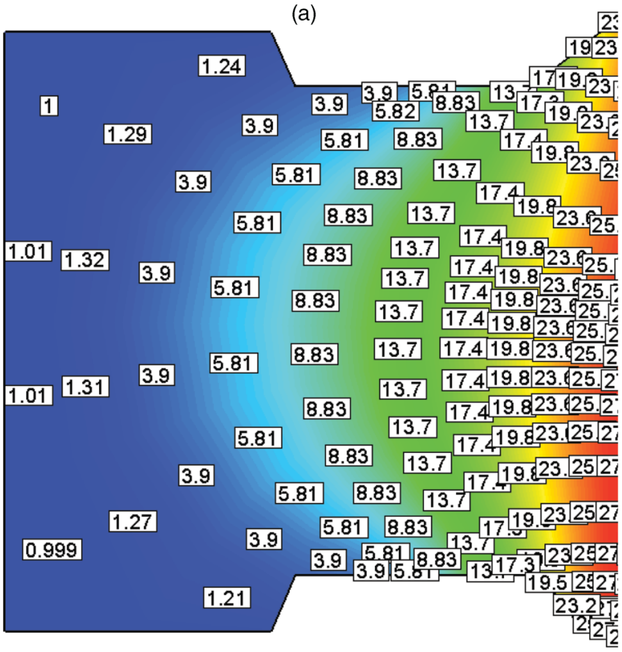

FIG. 13. (Color online) Effects of electron energy losses due to excitation and sheath BC for the convective electron heat flux at the anode. A Dirichlet BC, $\phi = V_A$, is imposed for the anode potential. (a) Only ionization losses and Dirichlet BC for the electron temperature (set at $T_e = 1$ eV). (b) With excitation losses and sheath BC [Eq. (30)] at the anode. The contours and boxed values depict electron temperature in eV.

with magnetic field curvature that is not highly convex towards the anode, as in SPTs, for example. In more advanced thrusters, such as the commercial thruster simulated here, the near-anode field lines are highly convex. In such cases the quasi-1D-based meshing imposes the extrapolated solution to a significantly larger portion of the near-anode region, thereby offering little insight on the driving physics there.

The comparisons show similar solutions but with some marked differences. The overall heating of electrons appears to be in close agreement between the two solutions, which is expected since the peak electron temperature and its spatial variation near this maximum are driven mainly by resistive heating that is dominated by ν_α; at $z/L \approx 1$, ν_α exceeds the classical collision frequency by more than one order of magnitude. Near the anode the electron temperature in Hall2De is driven largely by the imposed Dirichlet BC.

A notable distinction between the solutions for the electron number density and plasma potential is evident in the anode region, Fig. 10 (bottom). Hall2De yields a higher plasma density in this region with values for $z/L < 0.2$ exceeding by one order of magnitude those obtained by HPHall. A comparison of the terms in Eq. (45) shows that the anode region is dominated by ion diffusion since this is where the electric field is negligible. It is noted that as part of the inherent assumptions associated with the PIC simulation of ions the ion drag terms [numbered as “IV” in Eq. (45)] are not accounted for in HPHall. The ion pressure is also excluded in HPHall and the Hall2De simulations confirm this to be a good approximation for the assumed ion temperature of 500 °C. The comparison of all the ion momentum terms in steady state is shown in Fig. 12-right. In Eq. (45) ν_{in} is the ion-neutral charge-exchange collision frequency and $\mathbf{u}_n$ is the average drift velocity of neutrals.

$$\frac{\partial \mathbf{u}_i}{\partial t} \approx \underset{\text{(I)}}{\frac{q_i}{m_i}\mathbf{E}} + \underset{\text{(II)}}{(-\mathbf{u}_i \cdot \nabla)\,\mathbf{u}_i} + \underset{\text{(III)}}{\frac{-\nabla p_i}{n_i m_i}} + \underset{\text{(IV)}}{\left(\nu_{\text{in}} + \nu_{en}^{I}\right)(\mathbf{u}_n - \mathbf{u}_i)}. \qquad (45)$$

A related effect is associated with the variation of the electric field in this region where measurements have suggested little to no variation of the plasma potential (i.e., $E_z \approx 0$) [46]. Similar comparisons as those performed for the ion momentum may be carried out for the dominant terms in Ohm’s law, namely between the resistive and electron pressure terms. These comparisons suggest that the higher plasma density reduces significantly the importance of these terms in this region such that any differences between them [the numerator in Eq. (46)], that would otherwise generate a finite electric field, are reduced. The numerator in Eq. (46) is reduced further by comparison to the HPHall solution since the total classical collision frequency is higher (first term) and the density gradient is lower (second term). The e-i collision frequency (ν_{ei}) is found to be higher in the near-plume regions as well, in part due to the higher plasma density there but largely as a result of accounting for the multiply charged ions in Eq. (21) (through Z^*).

$$\begin{aligned} E_\perp &\approx \eta\left(1 + \Omega_e^2\right) j_{e\perp} - \frac{\nabla_\perp p_e}{e n_e} \\ &\sim n_e^{-1}\left[j_{e\perp} B^2/m_e\,(\nu_{ei} + \nu_{en}) - T_e \nabla_\perp n_e\right]. \qquad (46) \end{aligned}$$

Finally, two other effects are discussed here both associated with the electron energy equation. With Dirichlet BCs at the anode, specifying the electron temperature at 1 eV and the plasma potential at $V_A = 300$ V, we find that by not allowing the excitation losses to affect directly the electron temperature

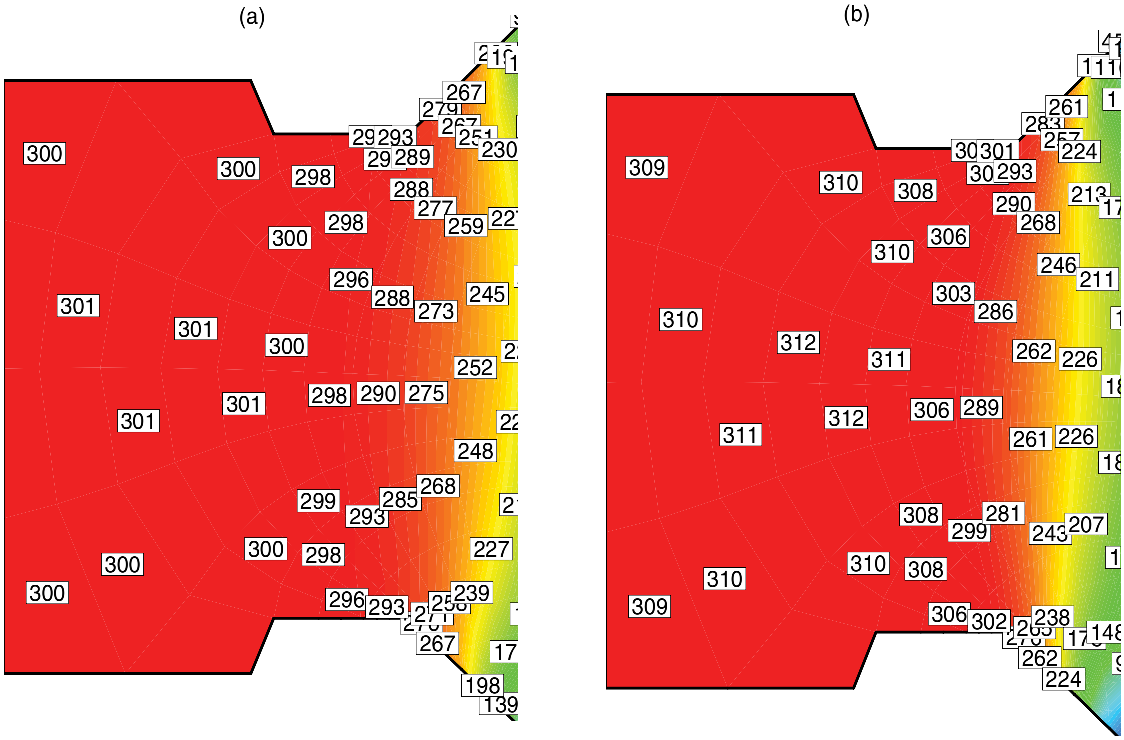

FIG. 14. (Color online) Effects of the sheath BC for the electron current density at the anode. Sheath BCs are imposed for the convective heat flux and excitation losses are included. (a) Dirichlet BC, $\phi = V_A$, imposed for the anode potential. (b) Sheath BC imposed for the electron current density [Eq. (29)]. The contours and boxed values depict plasma potential in V.

(since T_e is effectively held fixed by the imposed condition at the boundary), the consequence is a reduction of the plasma density. In reality, the presence of an electron-repelling sheath at the anode requires suitable BCs for both the electron current density [Eq. (29)] and the convective heat flux [Eq. (30)] that allow both T_e and ϕ to adjust self-consistently to flux losses through the sheath. The result of imposing Eq. (30) is shown in Fig. 13. We find that the plasma density remains relatively unchanged compared to those plotted in Figs. 10 and 12 but the electron temperature rises by ~2–3 eV in response to the reduction of convective heat loss by the electron-repelling sheath. In other words, we find that the impact of the sheath on the electron energy balance near the anode is more significant than the excitation losses.

The above-mentioned results set the anode potential at V_A. The second effect discussed here is related to the sheath BC for the electron current density, Eq. (29), and ultimately its impact on the anode potential. We find that the application of Eq. (29) leads to an increase in the plasma potential above the anode voltage V_A, which is to be expected since the electron thermal current to the anode is significantly higher than the electron current required by the discharge. In the hybrid-PIC simulations, the significantly lower (more than one order of magnitude) plasma density yields a proportionately lower j_{T_e} which leads to $\phi \lesssim V_A$ in this region. In the commercial thruster simulations with Hall2De we find the increase of the plasma potential to be $\lesssim$10 V as shown in Fig. 14. The electron temperature decreases by about 1 eV because the convective heat loss to the wall is now higher. This is because the contribution of $\Delta\phi = \phi - V_A$ in Eq. (30) is no longer zero. Ultimately, compared to the Hall2De solution in Fig. 10, only small differences in the plasma density near the anode are produced by the combined effects of sheath and excitation losses.

IV. CONCLUSION

This paper reports on the development of a 2D axisymmetric computational model of the ionized gas in Hall thrusters with the following main features: (1) resolution of electron transport parallel and perpendicular to the magnetic field, made possible by the discretization of the electron fluid equations on a MFAM, (2) large computational region in the plume that extends several times the channel size downstream of the thruster exit, (3) implicit solution for the conduction of electron current and heat, (4) solution of the hydrodynamic equations of continuity and momentum for isothermal ions, accounting for multiple charge states, charge-exchange collisions with neutrals and collisions between ions of different charge states, and (5) an algorithm for the neutrals that does not depend on discrete particles. The first feature has been implemented in part to permit channel erosion calculations in regions with complex magnetic field topologies but it also allows for the self-consistent solution of the near-anode plasma. Features (1) and (2) permit the self-consistent determination of the solution near the cathode. Our simulations have shown that the electron flow exhibits characteristics in this region that are purely two dimensional and cannot be resolved with a quasi-1D electron model. For example, we found that the assumption of isothermal lines of force is violated near the cathode. The large computational domain permits also the investigation of large-scale effects associated with the transport of electrons in the plume region of the accelerator. Larger time steps may be taken with the implicitization of the conductive terms. Features (4) and (5) yield "quiet" simulations of Hall thrusters by eliminating the statistical noise that is inherent in discrete-particle methods.

Results from benchmark simulations of a commercial Hall thruster suggest that the anode region is dominated by ion diffusion and the electric field is predicted to be negligibly small there, which is in agreement with plasma measurements. Mainly due to ion drag forces, the results show a significantly higher plasma density in this region by comparison to the hybrid-PIC simulation results of HPHall, which do not account for such forces. The combination of anode sheath boundary conditions, excitation electron energy losses, and self-consistent determination of the plasma properties yields approximately two to three times higher electron temperature in the anode region. Because the plasma density in the anode region is significantly higher than that predicted by PIC simulations, the electron thermal current density is also higher. Consequently, the Hall2De simulations yield plasma potential values that exceed the anode voltage by a few percent.

ACKNOWLEDGMENTS

The authors wish to acknowledge Alex Mathers for providing the thruster specifications and Richard Hofer for the HPHall numerical simulation results.

[1] A. I. Morozov, Vestnik Akademii Nauk Sssr, 15 (1974).

[2] A. I. Morozov and I. V. Melikov, Zh. Tekh. Fiz. **44**, 544 (1974).

[3] B. I. Volkov, A. I. Morozov, A. G. Sveshnikov, and S. A. Iakunin, Fiz. Plazmy **7**, 245 (1981).

[4] M. Hirakawa and Y. Arakawa, in *Proceedings of the 32nd AIAA Joint Propulsion Conference, Lake Buena Vista, Florida* (American Institute of Aeronautics and Astronautics, Washington, DC, 1996), p. 3195.

[5] J. M. Fife, Ph.D. thesis, Massachusetts Institute of Technology, 1998.

[6] J. M. Fife, M. Martinez-Sanchez, and J. Szabo, in *Proceedings of the 33rd AIAA/ASMA/SAE/ASEE Joint Propulsion Conference, Seattle, WA* (American Institute of Aeronautics and Astronautics, Washington, DC, 1997), p. 3052.

[7] J. P. Boeuf and L. Garrigues, J. Appl. Phys. **84**, 3541 (1998).

[8] S. Barral and E. Ahedo, Phys. Rev. E **79**, 046401 (2009).

[9] D. J. Bohm, E. Burhop, and H. Massey, in *National Nuclear Energy Series, Manhattan Project Technical Section, Division I*, edited by A. Guthrie and R. K. Wakerling (McGraw-Hill, New York, 1949), Vol. 5, p. 13.

[10] F. I. Parra, E. Ahedo, J. M. Fife, and M. Martinez-Sanchez, J. Appl. Phys. **100**, 023304 (2006).

[11] E. Sommier, M. K. Scharfe, N. Gascon, M. A. Cappelli, and E. Fernandez, IEEE Trans. Plasma Sci. **35**, 1379 (2007).

[12] G. J. M. Hagelaar, J. Bareilles, L. Garrigues, and J. P. Boeuf, J. Appl. Phys. **91**, 5592 (2002).

[13] L. Garrigues, G. J. M. Hagelaar, C. Boniface, and J. P. Boeuf, J. Appl. Phys. **100**, 123301 (2006).

[14] A. I. Morozov and V. V. Savelyev, in *Reviews of Plasma Physics*, edited by B. B. Kadomtsev and V. D. Shafranov (Consultants Bureau, New York, 2000), Vol. 21, p. 203.

[15] M. Keidar, I. D. Boyd, and I. I. Beilis, Phys. Plasmas **8**, 5315 (2001).

[16] R. Marchand and M. Dumberry, Comput. Phys. Commun. **96**, 232 (1996).

[17] Z. Lin, T. S. Hahm, W. W. Lee, W. M. Tang, and R. B. White, Science **281**, 1835 (1998).

[18] A. M. Dimits, Phys. Rev. E **48**, 4070 (1993).

[19] M. J. Lebrun, T. Tajima, M. G. Gray, G. Furnish, and W. Horton, Phys. Fluids B **5**, 752 (1993).

[20] R. E. Wirz, Ph.D. thesis, California Institute of Technology, 2005.

[21] G. J. M. Hagelaar, Plasma Sources Sci. Technol. **16**, S57 (2007).

[22] I. Katz and I. G. Mikellides, J. Comput. Phys. **230**, 1454 (2011).

[23] B. A. Welander and K. H. de Grys, in *Proceedings of the 53rd JANNAF Propulsion Meeting, Monterey, CA* (Johns Hopkins University, Chemical Propulsion Information Analysis Center (CPIAC), Baltimore, 2005).

[24] R. R. Hofer, I. G. Mikellides, I. Katz, and D. M. Goebel, in *Proceedings of the 30th International Electric Propulsion Conference, Florence, Italy* (Electric Rocket Propulsion Society, Fairview Park, OH, 2007), p. 267.

[25] I. G. Mikellides, I. Katz, R. R. Hofer, D. M. Goebel, K. de Grys, and A. Mathers, Phys. Plasmas **18**, 033501 (2011).

[26] J. M. Haas, R. R. Hofer, D. L. Brown, B. M. Reid, and A. D. Gallimore, in *Proceedings of the 54th JANNAF Propulsion Meeting, Denver, CO* (Johns Hopkins University, Chemical Propulsion Information Analysis Center (CPIAC), Baltimore, 2007).

[27] W. Huang, B. Drenkow, and A. D. Gallimore, in *Proceedings of the 45th AIAA Joint Propulsion Conference, Denver, CO* (American Institute of Aeronautics and Astronautics, Washington, DC, 2009), p. 5355.

[28] J. S. Miller, S. H. Pullins, D. J. Levandier, Y.-h. Chiu, and R. A. Dressler, J. Appl. Phys. **91**, 984 (2002).

[29] B. M. Reid and A. D. Gallimore, in *Proceedings of the 44th AIAA Joint Propulsion Conference, Hartford, CT* (American Institute of Aeronautics and Astronautics, Washington, DC, 2008), p. 4920.

[30] G. W. Sutton and A. Sherman, *Engineering Magnetohydrodynamics* (McGraw-Hill, New York, 1965).

[31] K. U. Riemann, J. Phys. D: Appl. Phys. **24**, 493 (1991).

[32] J. G. Andrews and R. H. Varey, J. Phys. A: Gen. Phys. **3**, 413 (1970).

[33] I. G. Mikellides, D. M. Goebel, J. S. Snyder, I. Katz, and D. A. Herman, J. Appl. Phys. **108**, 113308 (2010).

[34] I. G. Mikellides, I. Katz, D. A. Goebel, K. K. Jameson, and J. E. Polk, J. Propul. Power **24**, 866 (2008).

[35] E. Y. Choueiri, Phys. Plasmas **8**, 1411 (2001).

[36] N. B. Meezan, W. A. Hargus, and M. A. Cappelli, Phys. Rev. E **63**, 026410 (2001).

[37] D. Sydorenko, I. Kaganovich, Y. Raitses, and A. Smolyakov, Phys. Rev. Lett. **103**, 145004 (2009).

[38] S. I. Braginskii, in *Reviews of Plasma Physics*, edited by M. A. Leontovich (Consultants Bureau, New York, 1965), Vol. 1, p. 205.

[39] J. V. J. Dugan and R. J. Sovie, NASA Glenn Research Center, 1967, p. 50.

[40] G. D. Hobbs and J. A. Wesson, Plasma Phys. **9**, 85 (1967).

[41] O. Schenk and K. Gartner, Electron. Trans. Numer. Anal. **23**, 158 (2006).

[42] O. Schenk, A. Wachter, and M. Hagemann, Comput. Optim. Appl. **36**, 321 (2007).

[43] C. K. Birdsall, A. B. Langdon, J. P. Verboncoeur, and V. Vehedi, *Plasma Physics via Computer Simulation* (Adam Hilger, Bristol, UK, 1991).

[44] G. A. Bird, *Molecular Gas Dynamics and the Direct Simulation of Gas Flows* (Clarendon Press, Oxford University Press, Oxford, New York, 1998).

[45] A. Van Oosterom and J. Strackee, IEEE Trans. Biomed. Eng. **30**, 125 (1983).

[46] B. M. Reid, Ph.D. thesis, University of Michigan, 2009.